Available online at www.sciencedirect.com
ScienceDirect
Journal of Power Sources 173 (2007) 550–555
JOURNAL OF POWER SOURCES
www.elsevier.com/locate/jpowsour

Short communication

Synthesis and electrochemical properties of layered $LiNi_{2/3}Sb_{1/3}O_2$

Xiaohua Ma, Kisuk Kang, Gerbrand Ceder, Ying Shirley Meng *

Department of Materials Science and Engineering, Massachusetts Institute of Technology, 77 Massachusetts Avenue, Cambridge, MA 02139, United States

Received 12 June 2007; accepted 3 July 2007
Available online 24 July 2007

Abstract

$LiNi_{2/3}Sb_{1/3}O_2$ has been prepared by ion-exchange from $NaNi_{2/3}Sb_{1/3}O_2$. Powder X-ray diffraction (XRD) and single crystal electron diffraction by transmission electron microscopy (TEM) of the material indicate that it is isostructural with α-$NaFeO_2$. Electrochemical test shows that the reversible capacity for Li intercalation and deintercalation drops rapidly with the number of times cycled. Both experimental evidences and first principles calculations point to the migration of nickel as the reason for the poor capacity retention.

Keywords: Lithium ion battery; Ion-exchange; Antimony; Layered oxide

1. Introduction

Several Li intercalation electrodes with composition $LiNi_xTM_{(1-x)}O_2$ (TM = Ti, Mn) have been synthesized and evaluated. In these materials, only Ni participates in the electrochemical reaction while TM acts only as structure stabilizer [1–5]. A material such as $Li(Ni_{1/2}Mn_{1/2})O_2$ is perfectly balanced in extractable Li and electron content. Even though Mn^{4+} remains unchanged in valence, Ni^{2+} can be oxidized to Ni^{4+} thereby supplying all the electrons needed to extract Li^+. While this is ideal from a capacity perspective, it is likely that rate capability could be increased by adding more Ni^{2+} to the system. Li extraction from $Li(Ni_{1/2}Mn_{1/2})O_2$ creates Ni^{4+} which at high state of charge leads to a reduction in electronic conductivity [6]. Oxidation of Ni^{2+} to Ni^{4+} also leads to a significant increase in the activation barrier for Li hopping [7,8]. The electrostatic repulsion between Li^+ in its activated state and the transition metal ion has been shown to have a significant influence on the Li migration barrier [7–9]. In fact, Li motion in the presence of Ni^{2+} was found to have the lowest migration barrier of a series of common transition metal cations investigated in a recent computational study [8]. Hence, one would expect that increasing the Ni^{2+} content in layered $LiNi_xTM_{(1-x)}O_2$ materials could lead to materials that have improved rate capability at high state of charge. Since the average valence of the transition metals TM in layered $LiTMO_2$ materials needs to be +3, more Ni^{2+} can only be accommodated by incorporation of high valent cations in the structure. Using a +5 cation such as Sb^{5+} increases the Ni content to 66% as in $LiNi_{2/3}Sb_{1/3}O_2$. Even when all Li is removed from this material there should still be 1/6 of residual Ni^{2+} present, and at a typical charge limit corresponding to removal of 2/3 Li [3,10,11] one-third of all Ni would still be Ni^{2+} assuming the other Ni ions have been oxidized to +4.

When synthesized through a solid state route $LiNi_{2/3}Sb_{1/3}O_2$ forms an orthorhombic structure with *Fddd* space group [12]. To create a layered structure we synthesized $LiNi_{2/3}Sb_{1/3}O_2$ through an ion-exchange route from $NaNi_{2/3}Sb_{1/3}O_2$. Since the layered $R\bar{3}m$ structure is stabilized by a large size difference between the alkali and the TM cations, it is more likely to form a layered structure with a larger alkali ion such as Na^+ [13,14]. Indeed, $NaNi_{2/3}Sb_{1/3}O_2$ has been synthesized with a solid state process by V. Nalbandyan, *et al.* and the structure was confirmed to be layered $R\bar{3}m$ [15]. Ion-exchange is a soft chemical approach performed at relatively low temperature so that only

* Corresponding author. Tel.: +1 617 252 1507; fax: +1 617 258 6534.
E-mail address: ysmeng@mit.edu (Y.S. Meng).

0378-7753/$ – see front matter © 2007 Published by Elsevier B.V.
doi:10.1016/j.jpowsour.2007.07.033

Na^+ is replaced by Li^+ with the rest of the structure intact. It is reasonable to expect a well-layered $LiNi_{2/3}Sb_{1/3}O_2$ with very little cation mixing through such a synthesis route.

2. Materials and methods

2.1. Synthesis of $NaNi_{2/3}Sb_{1/3}O_2$

$NaNi_{2/3}Sb_{1/3}O_2$ was prepared by solid state reaction from Na_2CO_3 (99.5%, Aldrich), Sb_2O_3 (99.9%, Alfa Aesar) and $Ni(OH)_2$ (61% Ni, Alfa Aesar). Stoichiometric amount of these starting materials were ball-milled for 12 h. After drying, the mixture was ground and pressed into a pellet. The pellet was heated in air for 24 h at three different temperatures (800, 900, and 1000 °C). The resulting products are compared and the optimized sodium precursor was chosen for ion-exchange.

2.2. Ion-exchange

The obtained powder was mixed with 10 times excess amount of the eutectic composition of $LiNO_3$ (99.9+%, ACROS) and LiCl (99.9+%, Mallinckrodt Baker). The mixture was heated at 280 °C for 8 h in air. After ion-exchange, the mixture was rinsed several times with distilled water and filtered to recover the powder. The resulting powder was dried overnight in the air.

2.3. X-ray diffraction and TEM

XRD patterns were collected using a Rigaku diffractometer equipped with Cu Kα radiation by step scanning in the 2θ range of 10–80°. Rietveld refinement and profile matching of the powder diffraction data were performed with Fullprof [16]. In the refinement, the oxygen occupancy is fixed to the default value of 2 for the layered structure with space group $R\bar{3}m$. For the lithium or sodium and transition layers, we restrict both the Ni, Sb and Li/Na occupancy on the 3*a* sites, and the Ni, Li/Na occupancy on 3*b* sites, to sum to 1.

Electron diffraction patterns were collected under an accelerating voltage of 200 keV on a JEOL 2010 microscope. The powders were suspended on a copper grid with lacey carbon.

2.4. Electrochemical properties

Electrochemical cells were configured in the following way: Li/1 M $LiPF_6$ in EC:DMC = 1:1/$LiNi_{2/3}Sb_{1/3}O_2$ with carbon black (15 wt%) used as conductive agent and polyethylenetetrafluoride (PTFE) (5 wt%) as binder. Cells were assembled in an argon-filled glovebox and cycled at room temperature using a Maccor 2200 operating in galvanostatic mode.

2.5. Calculation methodology

Energies are derived from first principles calculations based on density functional theory (DFT). The spin-polarized generalized gradient approximation, Perdue–Wang exchange correlation function, and the projector augmented-wave method were used as implemented in Vienna ab initio simulation package (VASP) [17]. A plane-wave basis with a kinetic energy cutoff of 370 eV was used. A reciprocal-space *k*-point grids of $5 \times 5 \times 3$ or $3 \times 3 \times 5$ was used depending on the size of the supercell considered. Structures were fully relaxed. The +U correction term in the Dudarev scheme was used with $U = 5.96$ for Ni only [18].

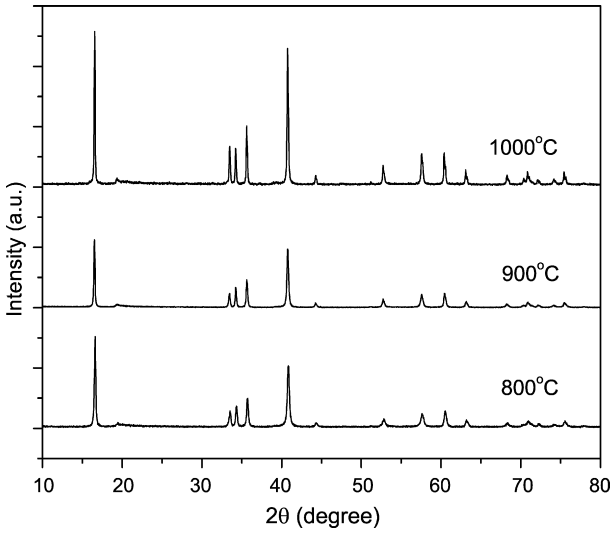

Fig. 1. XRD patterns of $NaNi_{2/3}Sb_{1/3}O_2$ synthesized at 800, 900 and 1000 °C.

3. Results and discussion

3.1. Structure of the precursor

XRD patterns for $NaNi_{2/3}Sb_{1/3}O_2$ precursors synthesized at three different temperatures 800, 900 and 1000 °C are shown in Fig. 1 and the results of the refinement are listed in Table 1. All three patterns can be well refined using the α-$NaFeO_2$ ($R\bar{3}m$) structure with Na in 3*b*(0, 0, 0.5) sites, transition metals (Ni, Sb) in 3*a*(0, 0, 0) sites and O in 6*c*(0, 0, *z*) sites. Both the Na occupancy and Na/Ni exchange are allowed to vary in the refinement. For $NaNi_{2/3}Sb_{1/3}O_2$ synthesized at 800 °C, the Na occupancy is 0.938 and the Na/Ni exchange is determined to be 0.9%. For the compound synthesized at 900 °C, the Na occupancy and Na/Ni exchange are 0.987% and 1%, respectively. For the Na phase precursor synthesized at 1000 °C, Na occupancy is 0.954 and the Na/Ni cation mixing is 4.5%. We choose the 900 °C material for ion-exchange as it has high Na occupancy with low Na/Ni exchange. The lattice parameters $a = 3.06$ Å, $c = 16.05$ Å

Table 1
Refinement results for $NaNi_{2/3}Sb_{1/3}O_2$ synthesized at three different temperatures

Synthesis temperature (°C)	Na occupancy (%)	Na/Ni inter-layer mixing (%)
800	93.8	0.9
900	98.7	1.0
1000	95.4	4.5

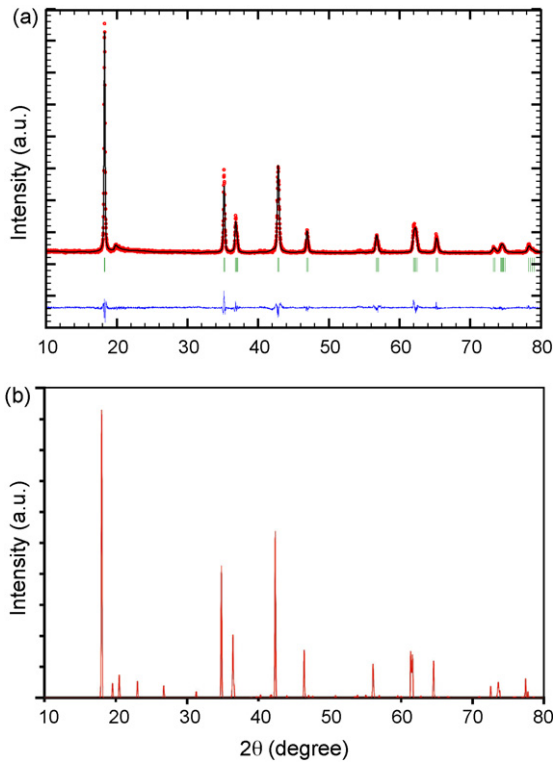

Fig. 2. (a) X-ray diffraction pattern and refinement of $LiNi_{2/3}Sb_{1/3}O_2$ obtained after 8h ion-exchange from $NaNi_{2/3}Sb_{1/3}O_2$ synthesized at 900 °C; (b) XRD pattern of $LiNi_{2/3}Sb_{1/3}O_2$ calculated by first principles methods with $\sqrt{3} \times \sqrt{3}$ ordering of Ni and Sb in the TM layer.

agree very well with the reported ones in reference [15], where $a = 3.06$ Å, $c = 16.02$ Å.

3.2. Structure of $LiNi_{2/3}Sb_{1/3}O_2$ after ion-exchange

The XRD pattern for $LiNi_{2/3}Sb_{1/3}O_2$ after ion-exchange is shown in Fig. 2(a). The difference between the observed and calculated XRD patterns for the $R\bar{3}m$ structure is also indicated. The Rietveld refinement (Table 2) gives a Li occupancy 0.973 which is a little bit lower than the Na amount in precursor. Also, the Li/Ni exchange is only 0.2%, which can essentially be neglected. The lattice parameters are $a = 2.99$ Å, $c = 14.56$ Å. Our XRD data indicates that the starting sodium precursor phase is not present anymore after the ion-exchange although a small amount of residual Na ions may still be present in the final material.

Table 2
Structure refinement parameters for $LiNi_{2/3}Sb_{1/3}O_2$ after ion-exchange at 280 °C

Atom	Site	*x*/*a*	*y*/*b*	*z*/*c*	Occupancy
Li(1)	3*b*	0	0	0.5	0.973
Ni(2)	3*b*	0	0	0.5	0.002
Ni(1)	3*a*	0	0	0	0.664
Li(2)	3*a*	0	0	0	0.002
Sb(1)	3*a*	0	0	0	0.333
O(1)	6*c*	0	0	0.25678	2.000

$a = 2.99$ Å, $c = 14.56$ Å, $R_p = 15.1\%$, $R_{wp} = 22.5\%$, $R_{exp} = 16.71\%$, $\chi^2 = 1.81\%$.

Fig. 3(a) and (b) shows two representative electron diffraction patterns from zone axes $[1\,\bar{1}\,\bar{1}]_{hex}$ and $[5\,1\,\bar{2}]_{hex}$ of the pristine $LiNi_{2/3}Sb_{1/3}O_2$, respectively. The fundamental reflections and the zone axes are indexed to the parent hexagonal cell with rhombohedral symmetry and space group $R\bar{3}m$. The $(1\,1\,l)(l = 3n)$ type fundamental reflections are clearly tripled with additional superstructure intensities, indicating that a $\sqrt{3} \times \sqrt{3}a_{hex}$ superstructure is present in $LiNi_{2/3}Sb_{1/3}O_2$. Ordering in a $\sqrt{3} \times \sqrt{3}a_{hex}$ supercell is common on a triangular lattice at composition 1/3 [19] and has also been speculated to occur in $LiNi_{1/2}Mn_{1/2}O_2$ with 10–12% Li/Ni interlayer mixing [20]. The ordering pattern is a honeycomb of Ni^{2+} with Sb^{5+} in the center of the honeycomb thereby maximizing the Ni^{2+}/Sb^{5+} nearest neighbor contacts.

We also investigated the structure of $LiNi_{2/3}Sb_{1/3}O_2$ with first principles calculations. In our calculation, the transition metal layer is ordered in the $\sqrt{3} \times \sqrt{3}a_{hex}$ superstructure and no inter-layer cation mixing is considered. Computational details are the same as in previous work on related materials [5]. The calculated lattice parameters are $a = 3.015$ Å, $c = 14.709$ Å, which are within 1% of the experimental values. The simulated XRD pattern based on these parameters is shown in Fig. 2(b), and agrees very well with the experimental results. The small peaks around 20° in both experimental and calculated pattern are the result of the superstructure in the transition layer.

In $LiNi_{2/3}Sb_{1/3}O_2$ synthesized by solid state method [12], the structure is a rock salt superstructure in the orthorhombic space group *Fddd*, where the isolated SbO_6 octahedra share edges with 12 adjacent octahedra randomly occupied by Li or Ni. This arrangement maximize the Sb–Sb distances.

3.3. Electrochemical results

The theoretical capacity of $LiNi_{2/3}Sb_{1/3}O_2$ is 225.4 mAh g^{-1} assuming that all the lithium ions can be extracted. As shown in Fig. 4, we find a first discharge capacity around 92 mAh g^{-1} at C/20 rate, which is less than half of the theoretical capacity. After 10 charge/discharge cycles, the capacity drops to 38 mAh g^{-1}. Fig. 4 shows that the capacity decays rapidly in the first 10 cycles.

3.4. Structure degradation during electrochemical reaction

To investigate possible structural changes as the origin for the capacity degradation, XRD pattern for electrodes which have been cycled five times was collected. The XRD spectrum and refinement are shown in Fig. 5. The refinement results show that the Li/Ni inter-layer mixing grows from 0.2% to around 10.4%. This dramatic change in structure was also confirmed from TEM patterns. Fig. 3(c) and (d) shows the $[1\,8\,2]_{hex}$ and $[\bar{2}\,5\,\bar{1}]_{hex}$ zone axes patterns collected from the sample in the discharged state after 10 charge/discharge cycles. The $\sqrt{3} \times \sqrt{3}a_{hex}$ superstructure is still present with somewhat enhanced intensities. Such phenomenon is observed in all ten crystals examined by TEM. Single crystal electron diffraction is known to be more sensitive to superstructure reflections than powder X-ray diffraction [21]. The superstructure peaks in XRD are completely diminished due to the amorphous carbonaceous additives and polymer binders

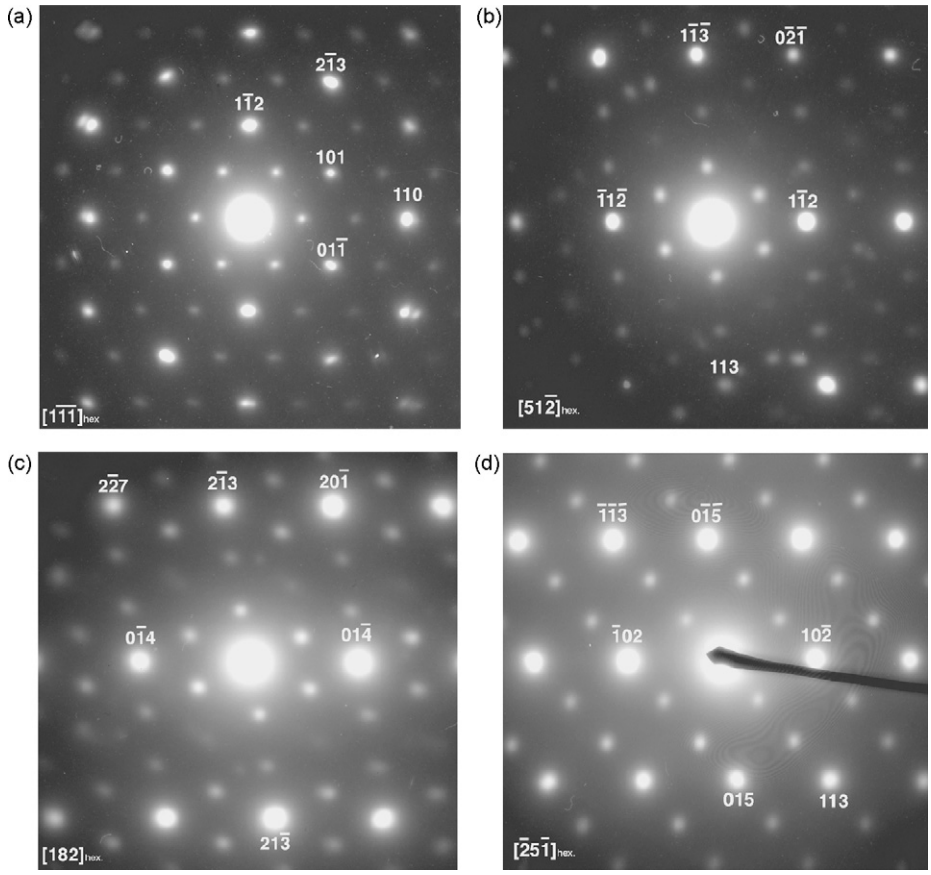

Fig. 3. (a) (b) TEM patterns for the pristine $LiNi_{2/3}Sb_{1/3}O_2$; (c) (d) TEM pattern for $LiNi_{2/3}Sb_{1/3}O_2$ after 10 cycles, in which the superstructure is enhanced.

in the electrode. Both XRD and TEM show that, although the pristine material has no cation mixing at all, once it is electrochemically cycled nickel will move into lithium layer.

To investigate whether Ni can migrate into Li vacancies, we calculated the activation barrier for Ni migration when the material is partially delithiated (Li concentration is 2/3). There are two possible pathways for the nickel migration: one is the most direct path travelling straight through the edge shared by neighboring octahedra; the other is a longer pathway where nickel goes through a nearest neighboring tetrahedral site via the faces it shares with the neighboring octahedra. Our previous work has consistently shown the tetrahedral path O_h–T_d–O_h to be substantially lower in energy than the direct octahedral hop for any ion migration in layered structures [1,9,22]. Fig. 6 demonstrates the migration pathway. One nickel migrates into the tetrahedral site through the triangular face between the TM layer and Li layer. A Li trivacancy around this tetrahedral defect is necessary to prevent face sharing of Li and the Ni tetrahedral defect. Meanwhile, one Li will move to the tetrahedral site that face-shares with the octahedral TM site vacated by

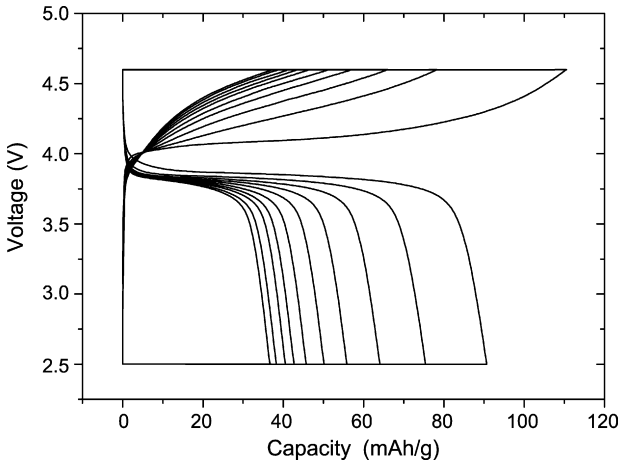

Fig. 4. Charge and discharge capacity for first ten cycles measured at C/20 rate. The voltage window is 2.5–4.6 V.

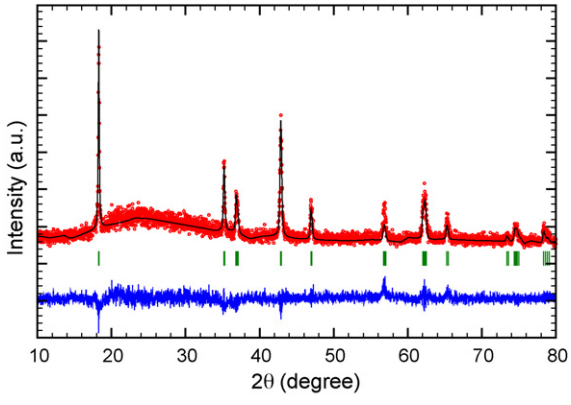

Fig. 5. XRD results of $LiNi_{2/3}Sb_{1/3}O_2$ electrode after five cycles. The Rietveld refinement indicates that cation mixing is around 10.4%.

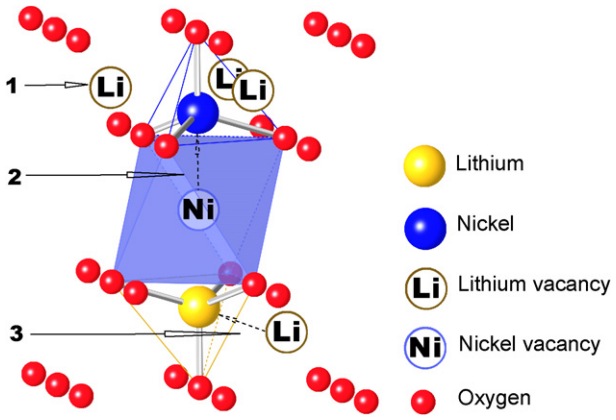

Fig. 6. Demonstration of the nickel migration and the formation of a Li/Ni dumbbell. The process can be divided into three steps: (1) Li disorder in a partially delithiated structure creates a trivacancy around a tetrahedron in the Li layer. (2) A single Ni ion moves from the TM layer into the triangular face between the TM and Li layer, and ultimately into the tetrahedral site of the Li layer. (3) The latter step is usually accompanied by one lithium moving into the tetrahedral site that shares a face with the octahedral site that has been vacated by the Ni ion. This leads to a Li_{tet}–Ni_{tet} dumbbell around the TM vacancy and is believed to be a key defect in $LiNi_{1/2}Mn_{1/2}O_2$ [10] and an intermediate state in the migration of Mn in $LiMnO_2$ [22].

Ni to lower the energy and form a Li/Ni dumbbell structure. We calculated the energy along this migration pathway in a $Li_8Ni_8Sb_4O_{24}$ unit cell with a $3 \times 3 \times 5$ k-point mesh. Fig. 7(a) shows that the energy barrier is around 0.63 eV. It is likely that this barrier is too low to keep the material stable. The Boltzmann success rate, $\exp(-0.63\,\text{eV}/k_BT) = 1.87 \times 10^{-11}$ at room temperature. Assuming a vibrational pre-factor of 10^{12} to 10^{13}/s, the Ni hopping rate would be around 20–200 s^{-1}. One may also compare this barrier to the Mn migration barrier in half delithiated Li_xMnO_2 (~0.4 eV) and the Co migration barrier in $Li_{1/2}CoO_2$ (~1.6 eV) [22]. Experimental evidence indicates that half delithiated Li_xMnO_2 will essentially transform into a spinel-like structure, while the $Li_{1/2}CoO_2$ layered structure remains stable due to the much higher migration barrier [23,24]. The Ni migration barrier in $LiNi_{2/3}Sb_{1/3}O_2$ is between that of Mn and Co but substantially closer to that of Mn in Li_xMnO_2. This seems further indication that some Ni will migrate into Li/vacancy layer resulting in a layered structure with high Li/Ni inter-layer mixing consistent with our XRD results. The Ni migration also explains the observation in electron diffraction (Fig. 3) that the $\sqrt{3} \times \sqrt{3}a_{hex}$ superstructure appears with somewhat enhanced intensities after cycling. When the material is cycled some Ni migrate into the lithium layer leaving the Ni sites vacated. Due to the larger contrast between Sb and a vacancy than between Sb and Ni, the superstructure in electron diffraction is enhanced.

In our calculations, the valence state of the migrating Ni can be determined by integrating the electron spin density in a sphere about the Ni cation centers [1,22]. Fig. 7(b) shows the net electron spin (in units of $1/2\mu_B$) as a function of the integration radius. The net spin rises fast initially as the 3d orbitals of Ni are integrated over. When the integration reaches the nonpolarized oxygen, however, the net spin levels off. The total spin (around 2 in units of $1/2\mu_B$) at the plateau in Fig. 7(b) indicates that the migrating Ni corresponds to a high spin Ni^{2+} ion. Our work on $LiNi_{1/2}Mn_{1/2}O_2$ has indicated that both the location of the Ni in the transition metal layer and the redox state of the Ni are critical factors that appear to control Ni motion [25]. In our layered $LiNi_{2/3}Sb_{1/3}O_2$, each Ni is surrounded by three Sb ions and three Ni ions. A Ni_{tet} site may be occupied or a Li/Ni dumbbell may form only when the Ni redox state is 2+, since both Ni^{3+} and Ni^{4+} have a strong preference for octahedral coordination [26]. If Ni is oxidized to 3+/4+ before migrating to a tetrahedral site, it becomes immobile. This may explain why not all Ni are prompted to migrate during charge and discharge. The comparatively lower migration barrier for Ni^{2+} in $LiNi_{2/3}Sb_{1/3}O_2$ than in $LiNi_{1/2}Mn_{1/2}O_2$ can be explained by the fact that the divalent Ni ion is surrounded by three Sb^{5+} and three Ni^{3+} when $LiNi_{2/3}Sb_{1/3}O_2$ is partially charged, and such strong electrostatic repulsion provides the driving force for the Ni^{2+} to migrate. It is important to realize the driving force may vary for Ni ions with different local environments and redox states. In fact, in previous first principles calculations on $LiNi_{1/2}Mn_{1/2}O_2$ we have shown that Ni^{2+} in the transition metal layer surrounded by six Mn^{4+} is unstable when it is oxidized to a higher redox state [25].

Using similar calculations, the possibility of Sb^{5+} migration in $Li_{2/3}Ni_{2/3}Sb_{1/3}O_2$ is also investigated. The calculated results

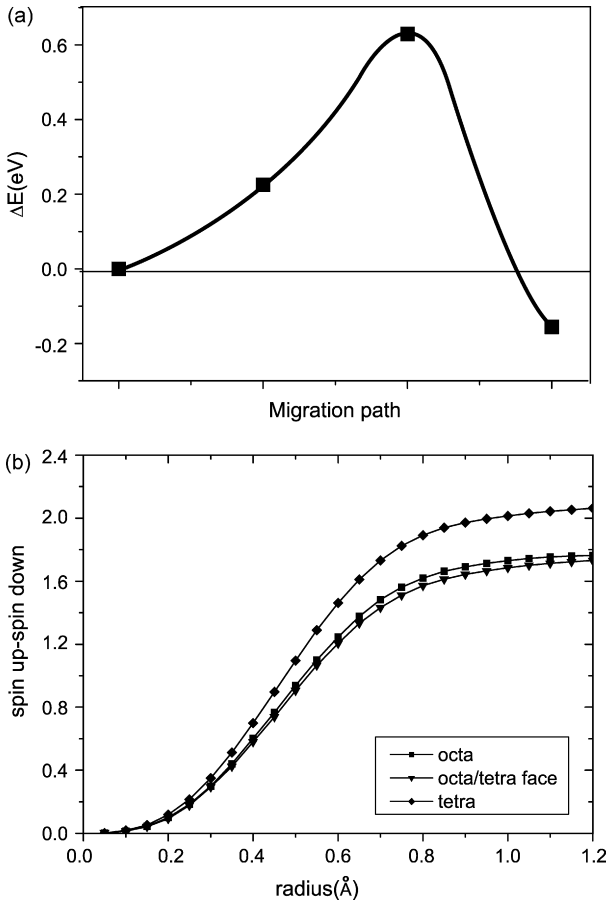

Fig. 7. (a) Energy for a Ni ion along the path from an octahedral site in the TM layer to a tetrahedral site in the Li/vacancy layer. (b) Integrated net spin for Ni cations along the migration path in $Li_{2/3}Ni_{2/3}Sb_{1/3}O_2$.

show that the energy required to create a Li/Sb dumbbell is about 1.5 eV making Sb^{5+} migration essentially impossible.

3.5. Relations between structure degradation and capacity decay

The Li/Ni dumbbell structure in partially delithiated electrodes can influence the electrochemical properties in two ways. Firstly, occupation of a tetrahedral site in the lithium layer by nickel requires that the nearest three octahedral sites are always vacant thereby reducing the insertion capacity. Additionally, the most likely pathway for lithium diffusion is identified as octahedral–tetrahedral–octahedral [9,27] so that stable Li/Ni dumbbells will block some possible lithium diffusion pathways. Hence, both the capacity and rate capability may be reduced by the formation of Li/Ni dumbbell.

4. Conclusion

Layered $LiNi_{2/3}Sb_{1/3}O_2$ was successfully synthesized by ion-exchange from $NaNi_{2/3}Sb_{1/3}O_2$ and tested in Li half-cells. Both experimental and computational results imply that nickel migrates from the transition metal layer to the Li layer when the material is partially delithiated, leading to rapid capacity fade.

Acknowledgements

This work was supported by the Assistant Secretary for Energy Efficiency, Office of FreedomCAR and Vehicle Technologies of the US Department of Energy under contract No. DE-AC02-05CH11231, via subcontract No. PO 6806960. We also acknowledge the support by the Center for Materials Science and Engineering at MIT under contract No. DMR-0213282. Valuable discussion with Prof. C.P. Grey is acknowledged. X.H. Ma would like to thank Y. Hinuma and B. Kang for their fruitful discussions.

References

[1] J. Reed, G. Ceder, Electrochem. Solid State Lett. 5 (7) (2002) A145.
[2] Z. Lu, D.D. MacNeil, J.R. Dahn, Electrochem. Solid State Lett. 4 (2001) A191.
[3] T. Ohzuku, Y. Makimura, Chem. Lett. 744 (2001).
[4] B. Ammundsen, J. Paulsen, J. Adv. Mater. 13 (2001) 943.
[5] K. Kang, D. Carlier, J. Reed, E.M. Arroyo, G. Ceder, L. Croguennec, C. Delmas, Chem. Mater. 15 (2003) 4503.
[6] S. Kumar, H.L. Li, J. Breger, C.P. Grey, Y. Shao-Horn, International Meeting on Lithium Batteries (IMLB) 13, Biarritz, France, 2006.
[7] K. Kang, Y.S. Meng, J. Breger, C.P. Grey, G. Ceder, Science 311 (2006) 977.
[8] K. Kang, G. Ceder, Phys. Rev. B 74 (9) (2006) 094105.
[9] A. Van der Ven, G. Ceder, Electrochem. Solid State Lett. 3 (2000) 301.
[10] J. Breger, Y.S. Meng, Y. Hinuma, S. Kumar, K. Kang, Y. Shao-Horn, G. Ceder, C.P. Grey, Chem. Mater. 18 (2006) 4768.
[11] Y. Makimura, T. Ohzuku, J. Power Sources 119–121 (2003) 156.
[12] G.C. Mather, R.I. Smith, J.M.S. Skakle, J.G. Fletcher, M.A. Castellanos, M.P. Gutierrez, A.R. West, J. Mater. Chem. 5 (8) (1995) 1177.
[13] E.J. Wu, P.D. Tepesch, G. Ceder, Philos. Mag. B 77 (1998) 4.
[14] T.A. Hewston, B.L. Chamberland, J. Phys. Chem. Solids 48 (1987) 97.
[15] V. Nalbandyan, I. Shukaev, O. Smirnova, ICDD PDF#00-0530344 (2002).
[16] Fullprof available at the following URL: http://www-llb.cea.fr/fullweb/fp2k/fp2k.htm.
[17] G. Kresse, J. Furthmuller, Comput. Mater. Sci. 6 (1996) 15.
[18] F. Zhou, M. Cococcioni, C.A. Marianetti, D. Morgan, G. Ceder, Phys. Rev. B 70 (2004) 235121.
[19] G. Ceder, A. Van der Ven, Electrochem. Acta 45 (1999) 131.
[20] Y.S. Meng, G. Ceder, C.P. Grey, W.-S. Yoon, M. Jiang, J. Breger, Y. Shao-Horn, Chem. Mater. 17 (2005) 2386.
[21] B. Fultz, J.M. Howe, Transmission Electron Microscopy and Diffractometry of Materials, 2nd ed., Springer.
[22] J. Reed, G. Ceder, Chem. Rev. 104 (2004) 4513.
[23] H. Wang, Y.-I. Jang, B. Huang, D.R. Sadoway, Y.-M. Chiang, J. Electrochem. Soc. 146 (1999) 473.
[24] H. Gabrisch, R. Yazami, B. Fultz, J. Power Sources 119 (2003) 674.
[25] Y. Hinuma, Y.S. Meng, K. Kang, G. Ceder, Chem. Mater. 19 (2007) 1790.
[26] B.N. Figgis, M.A. Hitchman, Ligand Field Theory and its Applications, Wiley-VCH, 2000.
[27] A. Van der Van, G. Ceder, J. Power Sources 97 (2001) 529.